UC San Diego

UC San Diego Previously Published Works

Title

Manipulating optical nonlinearities of molecular polaritons by delocalization.

Permalink

https://escholarship.org/uc/item/8kk210k6

Journal

Science advances, 5(9)

ISSN

2375-2548

Authors

Xiang, Bo
Ribeiro, Raphael F
Li, Yingmin
et al.

Publication Date

2019-09-01

DOI

10.1126/sciadv.aax5196

Peer reviewed

eScholarship.org Powered by the California Digital Library
University of California

Manipulating Optical Nonlinearities of Molecular Polaritons by Delocalization

Bo Xiang[2]†, Raphael F. Ribeiro[1]†, Yingmin Li[2], Adam D. Dunkelberger[3], Blake B. Simpkins[3], Joel Yuen-Zhou[1], Wei Xiong[1,2]*

[1]*Department of Chemistry and Biochemistry, University of California, San Diego, La Jolla, CA, 92093*

[2]*Materials Science and Engineering Program, University of California, San Diego, La Jolla, CA,92093*

[3]*Chemistry Division, Naval Research Laboratory, Washington, District of Columbia,20375*

Optical nonlinearities – how light-matter interactions are influenced by previous interactions with photons, are key resources in the contemporary photonics toolbox, relevant to quantum gate operations and all-optical switches. Optical nonlinearities of materials are often controlled at the microscopic level by chemical modification, which makes on-the-fly manipulation of such response challenging. Tunability of optical nonlinearities in the mid-IR is even less developed, hindering its applications in chemical sensing or IR photonic circuitry. Here, we report control of vibrational polariton coherent nonlinearities by manipulation of macroscopic parameters such as cavity longitudinal length or molecular concentration. These emergent nonlinearities last for the lifetime of the cavity mode, and subsequently evolve into the response determined by an incoherent population of dark reservoir modes. The observed phenomena arise due to the nonlinear macroscopic polarization stemming from strong coupling between microscopic molecular excitations and a macroscopic photonic cavity mode.

INTRODUCTION.

Molecular polaritons are hybrid quasiparticles resulting from strong coupling between molecular excitations[1–3] and microcavity electromagnetic modes, e.g. Fabry-Pérot (FP) cavity modes. Heuristically, polaritons arise when a cavity photon mode interconnects the microscopic molecular degrees of freedom, rendering their wavefunction coherently delocalized across a macroscopic length scale. This interplay between microscopic and macroscopic characteristics is at the heart of the versatility of polaritons. Much of the research on molecular polaritons has focused on modifying molecular properties through the interaction with the optical cavity[4–19]. Conversely, control of optical properties of polaritons via manipulation of macroscopic parameters defining the electromagnetic modes (e.g., cavity length) has received far less attention[5] (Fig.1a) and, in fact, we are not aware of any investigations of these effects in the nonlinear photonic regime. Here, we report qualitatively distinct regimes for polariton nonlinear response, and show that convenient macroscopic manipulation of polariton nonlinearities is achievable by controlling the cavity. The ease and versatility of such operation may make it applicable to in-situ control of optical nonlinearities for photonic circuitry and quantum information processing applications[20–22].

RESULTS.

Polariton Bleach Dependence on Cavity Longitudinal Length. To investigate the optical nonlinearities of vibrational polaritons, we measure their third-order nonlinear susceptibilities by femtosecond IR pump-probe spectroscopy. The hybrid light-matter system consists of a FP microcavity hosting an ensemble of asymmetric carbonyl stretch modes originating from $W(CO)_6$ molecules in a hexane solution[14]. At zero waiting time, when IR pump and probe pulses overlap, we see a significant reduction in the intensity of the polariton transmission (Fig.1b, c). This reduction gives rise to absorptive features in the pump-probe spectra. Qualitatively, this behavior resembles the well-known "photon blockade effect" in the single-emitter

†These authors contributed equally.

quantum regime of the Jaynes-Cummings model[23–30]: when a photon excites the emitter-cavity system, the latter is blocked from further interactions with incoming photons of the same frequency, thus leading to a reduction in photon transmission. Here, we observe a similar effect, but in the ensemble regime. However, as we discuss later, the mechanism for the reduced transmission at the ensemble level ensemble is quite different from that for a single-emitter. Thus, we term the phenomenon reported here as a "polariton bleach" and this phenomenon provides a foundation for developing mid-IR photonic devices in the ensemble regime of light-matter strong coupling.

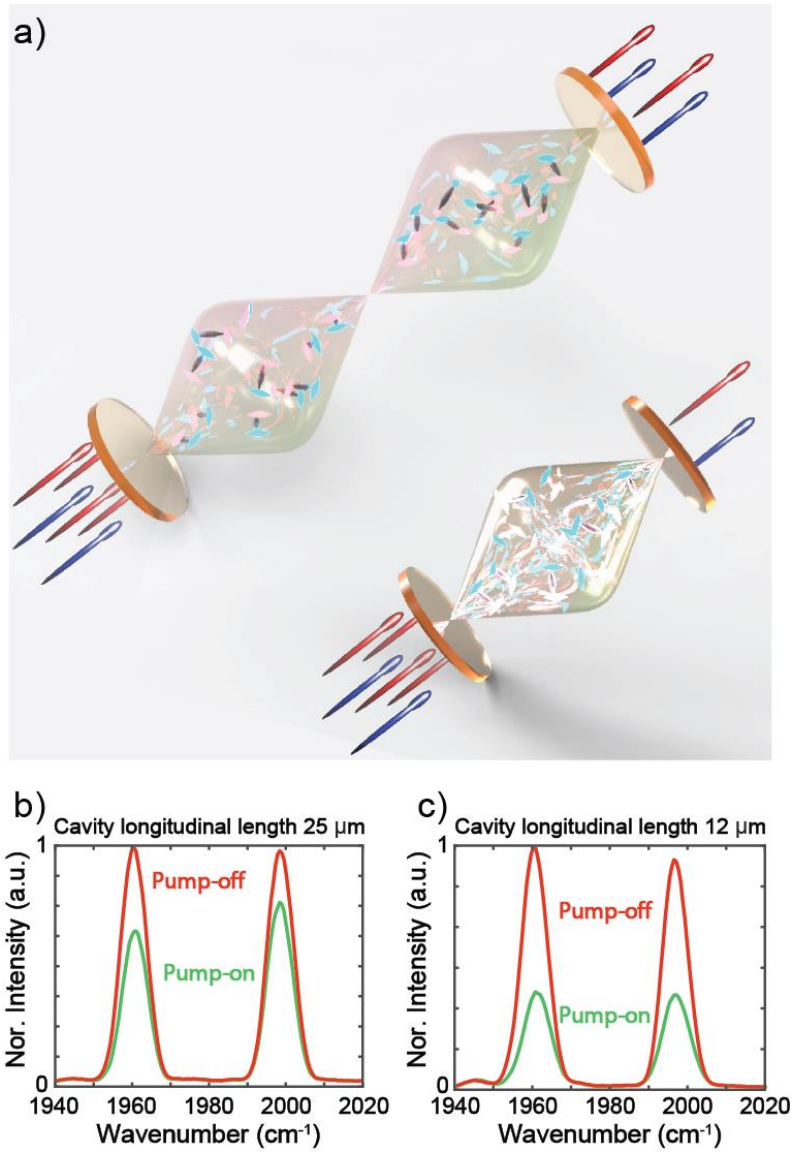

Figure 1. Polariton bleach effect at t_2 = 0 ps. (a) Key idea of optical nonlinearity manipulation via changes in the cavity thickness: by decreasing the cavity longitudinal length, the cavity volume is reduced, thus increasing polariton density, and therefore the polariton optical nonlinearity. The intensity of the bleach (difference of transmission intensity when pump is on and off) with (b) the 25 μm cavity gives much weaker polariton bleach than the (c) 12 μm. Notably, this effect is observed with a fixed molecular concentration, i.e., both systems have equal linear transmission spectra. Both systems have the same pump input (~10 mJ/cm^2) leading to similar polariton populations.

The polariton bleach effect shows peculiar dependence on cavity length: the bleach is stronger when the cavity longitudinal length is decreased and the concentration of $W(CO)_6$ is kept constant. In Figs. 1b and c,

we show that under these conditions, reducing the cavity spacer thickness from 25 to 12 μm, the percentage of polariton bleach is approximately doubled. This observation gives rise to the remarkable conclusion that substantially stronger nonlinearities are induced on molecular vibrational polaritons by merely changing the longitudinal length of the optical microcavity. Importantly, the concentration of $W(CO)_6$ is kept constant so that the linear transmission spectra for both remain approximately the same (the polariton Rabi splitting is fixed within 1 cm^{-1}). Thus, this cavity thickness dependence is completely hidden in linear optical response measurements (as previously reported by Simpkins et al.[7]). At a first glance, this is a puzzling result given that a sample of independent molecules in the *weak* light-matter coupling regime features nonlinear optical signals (e.g., 3rd order to 1st order nonlinear susceptibility ratio) that remain unchanged upon scaling of system size, *i.e.*, it is an intensive property of the system. This breakdown of size scaling can be qualitatively understood as follows: at a fixed molecular concentration, while the *number* of polariton transitions accessed by the IR pulses is approximately the same in both samples (determined by the number of IR photons entering the cavity), the volume of the polariton wavefunctions is not. Thus, the *density* of polaritons driven and accessed by the pulses is lower in the larger volume sample, yielding a weaker nonlinear signal. As we discuss later and in more detail in the SM, this system-size dependence of the polariton bleach is also an unambiguous manifestation of the macroscopic delocalization of polariton states.

Origin of Polariton Bleach and its Rabi Oscillation Dynamics Revealed by 2D IR. To further understand the physical origin of the polariton bleach and its dependence on cavity longitudinal path length, we performed two-dimensional infrared (2D IR, Fig. 2a) spectroscopy on molecular vibrational polariton samples. 2D IR measures the third-order nonlinear optical response function of a material, providing detailed spectral and dynamical features[14,31–36] that are not observable in pump-probe spectra (Fig. 2 b and c). In particular, 2D IR can state-selectively excite and probe specific transitions, a feature which is critical to discern the nonlinear optical response induced by polariton or dark state excitations. In Fig. 2d, we show the 2D IR spectrum of vibrational polaritons (cavity thickness = 25 μm) at $t_2 = 0$ ps. Four absorptive peaks dominate the spectra: two lie along the diagonal while the remaining correspond to cross-peaks. The 2D IR spectra of polaritons formed with the 12 μm-cavity display qualitatively similar features (Fig.S3a). Spectral cuts of 2D IR that correspond to pumping specific polaritons (UP or LP) show that all peaks have absorptive lineshape. Furthermore, comparison of spectral cuts for polaritons with 12 and 25 μm cavity thickness (Fig. S9) demonstrates agreement with the pump-probe results – polaritons formed with the 12 μm cavity have stronger nonlinearities. We note that, due to heterogeneity, dark modes can also be weakly excited, and induce similar absorptive features[14,37]. Overall, the observed 2D IR spectral features and corresponding cavity longitudinal length dependence is consistent with the polariton bleach observed in the pump-probe data.

Additional insights on the origin of the polariton bleach can be obtained by further investigation of pump-probe and 2D IR spectral dynamics. First, both pump-probe and 2D IR at $t_2 = 0$ ps (Fig. 2b and 2d) show different spectral lineshapes from those measured at $t_2 = 25$ ps (Fig. 2c and e). At 25 ps, the peaks located at $\omega_3 = \omega_{LP}$ are much stronger than those at $\omega_3 = \omega_{UP}$, and the spectral shape centered around $\omega_3 = \omega_{UP}$ evolves into a derivative shape. As explained in previous work[11,14], these features may be viewed to arise from ground-state population bleach, or equivalently, by the existence of transient excited reservoir population. The large and small negative peaks at $\omega_3 = \omega_{LP}$ arise primarily from the interference of the LP transition with the stimulated emission and excited state absorption of dark reservoir state population. The dispersive lineshape at $\omega_3 = \omega_{UP}$ is a result of the Rabi splitting contraction induced by the bleaching of molecular absorbers. In contrast, the polariton bleach at $t_2 = 0$ ps has a qualitatively different lineshape with the feature at $\omega_3 = \omega_{UP}$ stronger and purely absorptive (see Supplementary Information S12). This provides

strong evidence that the physical phenomena governing vibrational-polariton dynamics at ultrafast times (<cavity lifetime, ~3 ps), are different from those governing behavior at longer times.

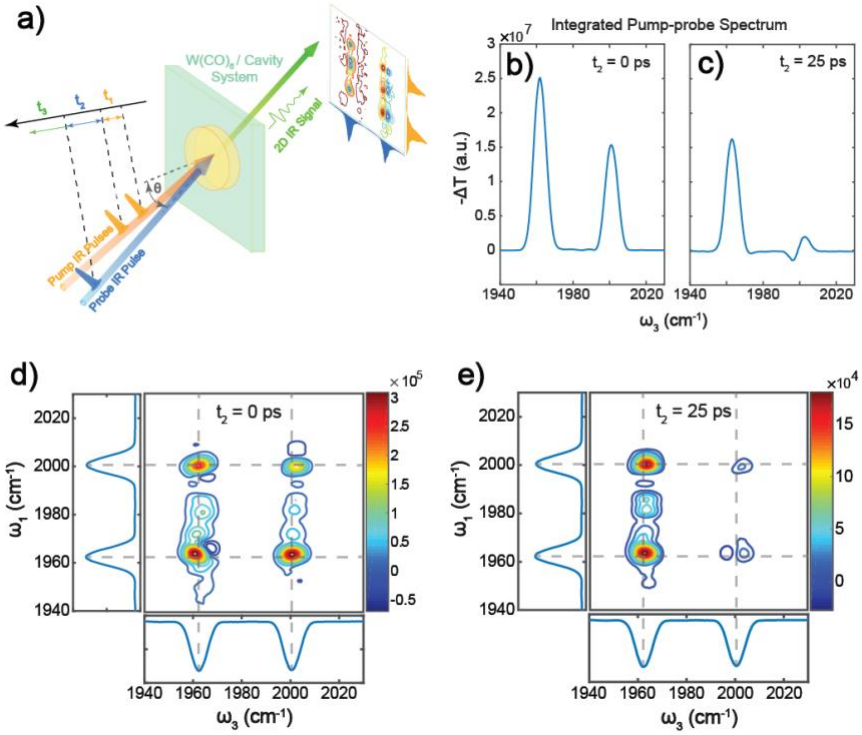

Figure 2. 2D IR spectroscopy of molecular vibrational polaritons. (a) Illustration of experimental setup. (b) and (c) pump probe early and late time delays. (d) and (e) 2D IR spectra of molecular vibrational polaritons at early and late time delays. Strong absorptive lineshapes are observed at early time delays.

The time-dependent dynamics extracted from 2D IR further confirm that the absorptive spectral signatures at early times and at 25 ps have different origins. The notable difference between early and late time dynamics is that at early times, e.g., when the pump-probe and 2D IR spectra features are absorptive, the spectra oscillate as a function of t_2. These oscillations are revealed in the t_2 dynamics of 2D IR spectral cuts at $\omega_1=\omega_{UP}$ (Fig. 3a) and ω_{LP} (Fig. S8). The oscillation period is c.a. 0.8 ps (41.7 cm^{-1} in frequency domain), which agrees well with the independently measured Rabi splitting of 38 cm^{-1}. Therefore, we assign these periodic dynamics to Rabi oscillations; the evolution of polariton coherences |UP><LP| and |LP><UP|, which is equivalent to energy exchange between the photon and the collective vibrational polarization in the local mode picture. In contrast, Rabi oscillations are absent from the dynamics of the spectral cuts taken at dark state reservoir frequencies further indicating, as expected, that no coherent oscillations occur with participation of these dark modes.

By applying a Fourier filter at the Rabi frequency to a series of t_2-dependent 2D IR spectra (see Supplementary Information S6), we extract an oscillatory component (referred to as AC) of the spectra during t_2 and isolate it from the non-oscillatory (DC) part. In Fig. 3b, we provide examples of AC and DC spectral cuts obtained from 2D IR spectra for the 25 μm cavity system at t_2 = 0.8 ps. The coherent AC features at the LP and UP frequencies are absorptive and have almost equal intensity matching the lineshape of the polariton bleach (Fig. 4a). Conversely, the DC spectra show a dispersive shape at the UP and much stronger nonlinear response at the LP, agreeing with our previous model[13,14] for late-time pump-probe response (Fig. 4b). Because the AC signal requires the evolution of quantum coherences |UP><LP| and |LP><UP| during t_2, the corresponding nonlinear resonances can be ascribed to a small subset of Feynman diagrams including coherence evolution (see Supplementary Information S7). Interestingly, this implies

that pathways containing polariton population (represented by |LP><LP| and |UP><UP|) are inessential for the generation of polariton bleach, i.e., |LP><UP| and |UP><LP| coherences are sufficient to induce polariton bleach. In summary, we identify two regimes of qualitatively distinct nonlinear polariton response: at early times (<3-4 ps, which is the dephasing time of the polaritons) one observes a bleaching of transmission occurring symmetrically at both polaritons that is essentially indistinguishable from the AC signal (Fig. 4a), and the late-times (>3-4 ps) there is a time-dependent DC signal that arises from dark-state-reservoir population (Fig. 4b).

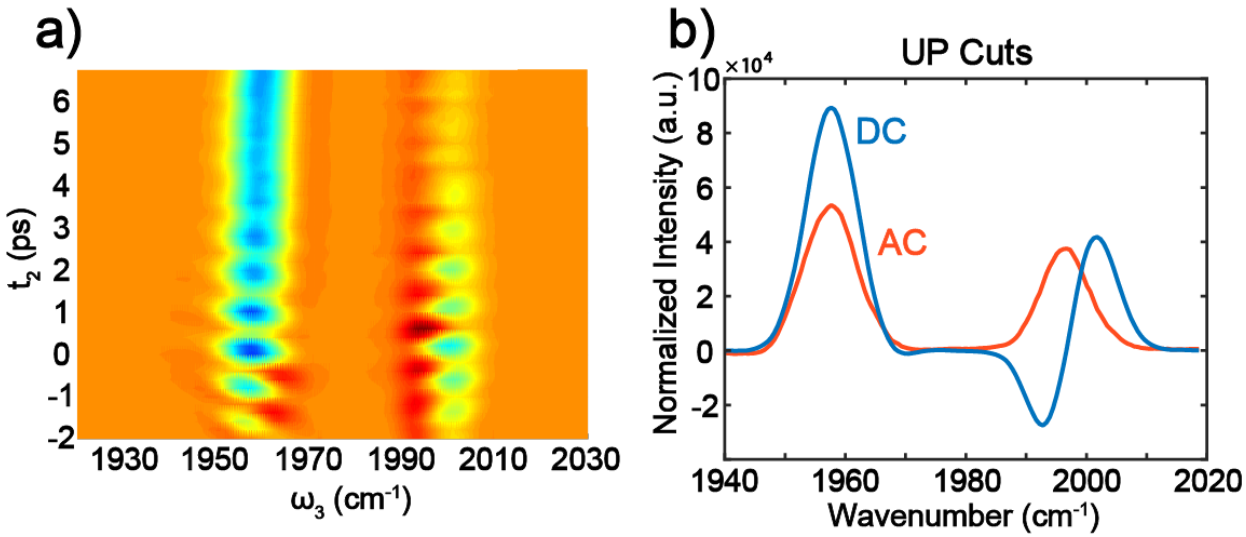

Figure 3. Rabi oscillations of 2D IR spectral cuts at $\omega_1=\omega_{UP}$ between -2 and 7 ps. (b) AC and DC spectral cuts at $\omega_1=\omega_{UP}$, showing an absorptive lineshape in the AC spectrum and a dispersive lineshape for the DC spectrum at t_2=0.8 ps

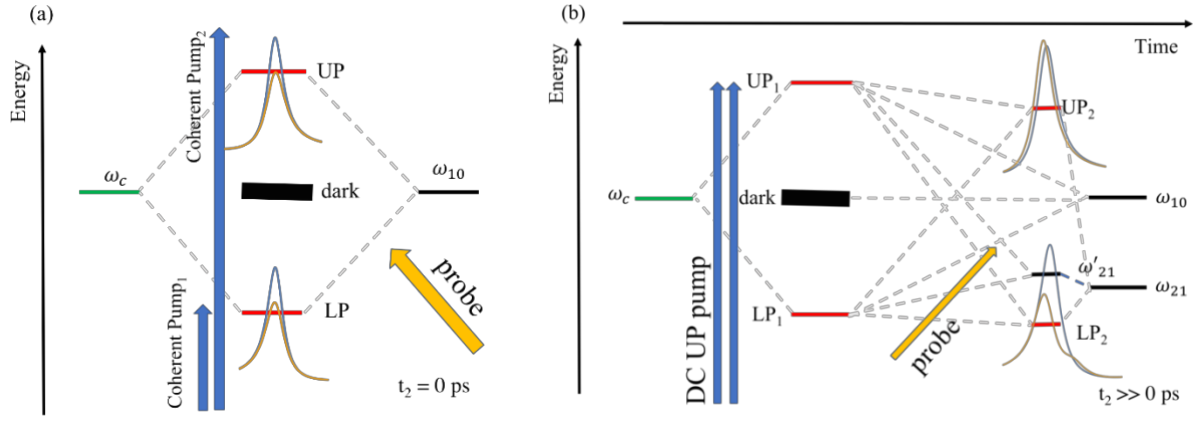

Figure 4. Energy level diagram representation of coherent (AC) and incoherent (DC) dynamics (a) Energy level diagram showing the processes giving rise to the polariton bleach and AC signal in Fig. 3, where pumping generates LP-UP coherences and thus Rabi oscillations, and polariton bleach is observed when the probe interacts with the system at short times (t_2 < 3-4ps) after pumping. Blue lineshapes represent linear response signals, while yellow show the polariton bleach effect. (b) Scheme showing the DC or long-time (t_2 >> 3ps) pump-probe response, where polariton population is generated and subsequent decay into the dark reservoir leads to changes in the collective oscillator strength due to a reduction in the average number of molecules in the ground-state. Blue lineshapes represent linear response signals and yellow give the pump-probe polariton lineshapes.

We find that the symmetric polariton bleach can be described with a semiclassical model[38] (see Supplementary Information S10). Given that the Rabi splitting does not change during this bleaching, there must be no loss of oscillator strength. Instead, we found broadening from 3 cm^{-1} to 4.8 cm^{-1} and from 3 cm^{-1} to 6 cm^{-1} reproduces the bleaching effect for 25 μm and 12 μm polaritons, respectively (Fig. 5). Thus, we propose that polariton coherences lead to probe transitions with a spectral signature that manifest a broadened polariton homogeneous linewidth and therefore reduced transmissions. This agrees with our supposition above, that only coherences are necessary for generating the polariton bleach. From a microscopic perspective, it is likely that strong polariton pumping (~10 mJ/cm^2) favors ultrafast vibrational dephasing pathways induced by many-body interactions which enhance dissipation and reduce transmission. Indeed, the polariton bleach effect also happens in inorganic semiconductor exciton-polaritons under high pumping[39–41]. In these systems, the rapid dephasing is induced by Coulomb interactions, which lead to enhanced broadening of the exciton homogeneous linewidth[38]. A similar mechanism has not yet been identified for vibrational-cavity polaritons as we report its first observation here. Future investigations will be carried out to investigate this phenomenon in detail, as it is out of the scope of this initial report.

Another way to explain the polariton bleach phenomena is via a quantum mechanical analysis using double-sided Feynman diagrams[42], as summarized in Supplementary Information S7. These Feynman diagrams

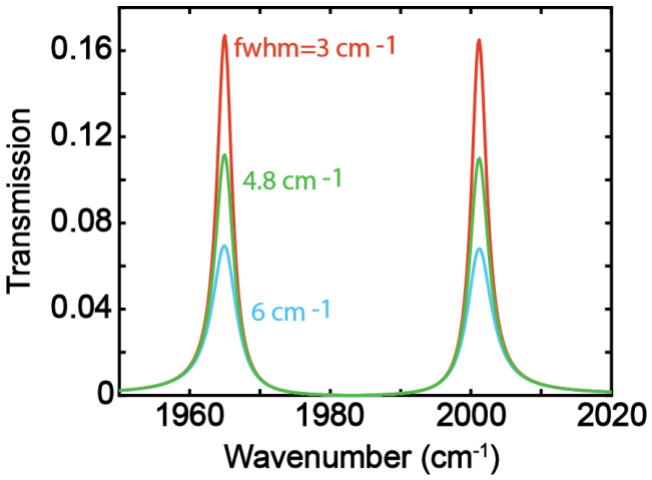

Figure 5. Simulated polariton transmission from a classical phenomenological model where the effect of the pump is to change the molecular homogeneous dephasing rate, here represented by fwhm. This process gives rise to enhanced polariton absorption and reduced transmission, reproducing the polariton transmission reduction in Fig. 1b and c.

represent the four peaks observed in 2D IR spectra. Each AC peak has a stimulated emission and an excited-state absorption (ESA) pathways involving fundamental |g>->|LP> (or |g>->|UP>) or combination band |UP>->|UP,LP> (or |LP>->|LP,UP>) transitions. The phases of these pathways are opposite in sign. Therefore, if they had equal absolute intensity, transition frequency and linewidths, such as in harmonic systems, their amplitudes would interfere destructively leading to a vanishing 2D IR signal. In nonlinear spectroscopy of regular molecular systems, the 2D signal is typically caused by the anharmonic shift in frequency of the ESA which leads to incomplete cancellation of the stimulated emission and ESA amplitudes. This paradigm does not apply to the observed polariton bleach, since no anharmonic energy shifts are apparent in this case; rather, the anharmonicity seems to be expressed in the linewidths, corresponding to nonlinear coupling to the environment. Specifically, there is an incomplete cancellation

of Feynman diagrams which is induced by a nonlinear dephasing mechanism that affects |LP,UP><LP| (|LP,UP><UP|) coherences, but does not act on |UP><g| (|LP><g|).

Lastly, we note that the inverse dependence between the polariton nonlinear response and the cavity length is also observed at later times (25 ps). This indicates that although the lineshape and nonlinear interactions in this regime are clearly different than at 0 ps, the inverse dependence of polariton nonlinearity is preserved. After 25 ps, the transient state of the cavity consists of some fraction of the molecules in the excited-state and the rest in the ground state. In this case, the cavity thickness dependence can be explained with the long time-delay pump-probe model described in our previous work[11]. The leading contribution to the nonlinear transmission of the probe at 25 ps is due to a population of molecules in the excited reservoir state, f_{pump}, within the photonic coherence volume[11,13,14]. The number of molecules in this volume increases quadratically with the cavity length[11], while the population of excited molecular modes grows linearly (see Supplementary Information S14). Therefore, f_{pump} for the 25 μm microcavity at 25 ps is smaller than the corresponding value for the 12 μm system by roughly a factor of two, which gives rise to the observed inverse dependence of the nonlinear response with cavity thickness. From our previous theory, the inverse dependence of polariton anharmonicity with respect to cavity coherence length observed at 25 ps arises from the local character of mechanical and electrical anharmonicity. We thus speculate that the similar inverse thickness dependence of polariton bleach at 0 ps is also induced by local molecular nonlinearities.

The Dependence of Polariton Bleach on Molecular Concentration.

To corroborate the hypothesis in the previous paragraph, we examined the polariton bleach effect as a function of concentration at a fixed 25 μm cavity thickness. Here, we focus on the transient signal at $\omega_3 = \omega_{UP}$ (Fig. 6), to avoid complications of the spectral peak at $\omega_3 = \omega_{LP}$ stemming from overlap with the 1-2 dark mode transition[11,13,14]. The UP peak intensities observed in 2D IR spectral cuts at ω_1 = LP and ω_1 = UP (normalized to linear transmission, in Fig 6, faded green areas) indeed provide evidence that the nonlinear dynamics generating the polariton bleach has inverse dependence on the total number of molecules within the cavity coherence length. This is a striking effect from the perspective of conventional nonlinear molecular spectroscopy in the weak light-matter coupling regime, where the nonlinear bleach to linear absorption ratio typically remains constant with increased molecular concentration (i.e., the molecules act as independent quantum emitters). In the strong-coupling regime, however, this assumption is clearly no

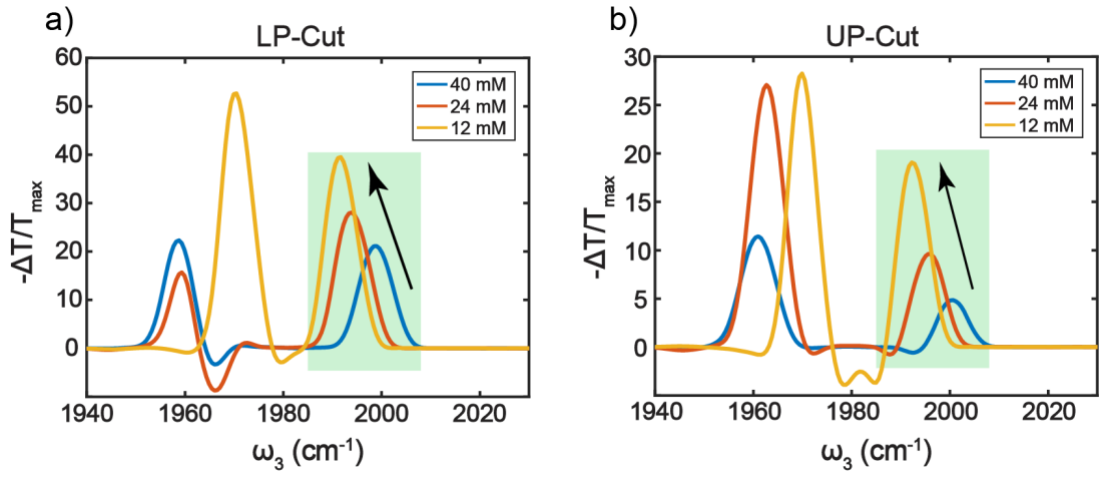

Figure 6. The polariton bleach effect at t_2 = 0 ps (optical nonlinearity) as a function of concentration. For both 2D-IR spectral cuts at (a) $\omega_1=\omega_{LP}$ and (b) $\omega_1=\omega_{UP}$, the bleach signal increases as the molecular concentration decreases.

longer valid, and an entirely new scaling of nonlinear interactions is in effect when varying cavity length and molecular concentration.

DISUSSION.

The observed polariton optical nonlinearity dependence on macroscopic properties (cavity longitudinal length and molecular concentration) is a result of the hybridization of molecular transitions with macroscopic cavity modes. The delocalization of polaritons makes their optical nonlinearities particularly sensitive to macroscopic parameters. We note that the reduced polariton transmission observed at short times can be phenomenologically attributed to the pump-induced nonlinear increase in polariton homogeneous linewidths. As the cavity volume and the number of molecules in the polariton coherence volume decrease, polariton nonlinearities become stronger. This trend agrees with the notion that in the limit of single emitter strong coupling (unattainable in our experiment), huge nonlinearities like single-photon blockade are expected.

The results reported in this article show novel nonlinear optical phenomena in the mid-IR regime that rely on a delicate interplay between microscopic molecular anharmonicities and macroscopic electromagnetic parameters. Multidimensional spectroscopy allows us to tease out the mechanism that drives the oscillating polariton bleach and unambiguously show that it depends on polariton coherences. The ease with which the described samples can be fabricated and handled at room-temperature, together with their unique effects that reside between molecular and photonic, make vibrational polaritons ideal platforms to design novel mid-IR nonlinear optical switches, to control chemical reactivity, or to serve as building blocks for quantum information processing applications. As an example, from our previous work[11,14], we know that polariton bleach and other nonlinear effects disappear within 200 ps. Thus, an all-optical modulator for mid-IR frequencies operating at repetition rate as high as 5 GHz can be developed based on the results reported here. This study has also evidenced that polariton nonlinearities can be straightforwardly tuned via macroscopic controls. One can envision exploring these ideas in the context of microfluidic devices so that molecular concentrations, and therefore, optical nonlinearities can be changed on-the-fly. Alternatively, polariton nonlinearities could be actively modified by combining cavities with piezo, thermal, and optically responsive materials[43–45], thus providing additional features to integrated photonic circuitry. Finally, the polariton anharmonicities underlying the respective nonlinearities may have nontrivial implications to vibrational dynamics and thermally-activated chemical reactions[46]. In summary, we envision the exotic nonlinearities explored in this work to play an important role in the emergent field of molecular polaritonics in the upcoming years.

METHODS.

Polariton Preparation. The $W(CO)_6$ (Sigma-Aldrich) /cavity system is prepared in IR spectral cell (Harrick) containing two dielectric CaF_2 mirrors separated by a 12 or 25 μm spacer and filled with $W(CO)_6$/hexane solution (concentration varies from 12 mM to 40 mM). The dielectric mirror has a ~96% reflectivity. Because the Rabi splitting (20 to 37 cm^{-1}) is larger than the full-width-at-half-max of both cavity (~11 cm^{-1}) and $W(CO)_6$ vibrational (~3 cm^{-1}) modes, the strong coupling criteria is satisfied.

Pump Probe and 2D IR Spectroscopy. The spectrometer follows the pulse shaper enabled pump-probe 2D IR setup and a rotational stage is added to control beam incidence angle. In the 2D IR spectrometer, three IR pulses interact with a sample sequentially to create two vibrational coherences. The first coherence is characterized by scanning t_1. The second coherence introduces a macroscopic polarization which subsequently emits a third order IR signal, which is self-heterodyned and detected in frequency domain. Transient pump-probe signal can be obtained by simply set $t_1 = 0$ fs, while to display 2D IR spectra, the FID in t_1 is numerically Fourier transformed.

Data availability.

The data that support the plots within this paper and other finding of this study are available from the corresponding author upon reasonable request.

Acknowledgements.

We thank Dr. Jeffery C. Owrutsky for insightful discussions. B.X., J.W., Y.L., W.X. are supported by AFOSR Young Investigator Program Award, FA9550-17-1-0094. B.X. thanks Roger Tsien Fellowship from UCSD Department of Chemistry and Biochemistry. The development of the theoretical model by R.F.R. is supported by AFOSR award FA9550-18-1-0289, while the analysis of the short time dynamics by R.F.R and J.Y.Z. was supported by NSF CAREER CHE 1654732.

Author Information.

Affiliations

Department of Chemistry and Biochemistry, University of California, San Diego, La Jolla, CA, 92093

Raphael F. Ribeiro, Joel Yuen-Zhou, Wei Xiong

Materials Science and Engineering Program, University of California, San Diego, La Jolla, CA,92093

Bo Xiang, Yingmin Li, Wei Xiong

Chemistry Division, Naval Research Laboratory, Washington, District of Columbia,20375

Adam D. Dunkelberger, Blake S. Simpkins

Contributions.

W.X. supervised the overall research and J.Y-Z. supervised the theoretical work. B.X. and W.X. designed the experiments. B.X., Y.L. conducted the experimental work. B.X. and W.X. analyzed experimental data. A.D.D., B.B.S. provided cavity optics. R.F.R. and J.Y-Z developed theoretical work. B.X., R.F.R., J.Y-Z. and W. X. interpreted the experimental and theory results. B.X., R.F.R., A.D.D., B.B.S., J.Y-Z. and W. X discussed the results and contributed to the final manuscript.

Competing interests.

The authors declare no competing interests.

Corresponding author

*Correspondence to Wei Xiong.

Supplementary information.

Supplementary notes and figures can be found in the supplementary information.

Reference:

1. Long, J. P. & Simpkins, B. S. Coherent coupling between a molecular vibration and fabry-perot optical cavity to give hybridized states in the strong coupling limit. *ACS Photonics* **2,** 130–136 (2015).

2. Ebbesen, T. W. Hybrid Light-Matter States in a Molecular and Material Science Perspective. *Accounts of Chemical Research* **49,** 2403–2412 (2016).

3. Shalabney, A. *et al.* Coherent coupling of molecular resonators with a microcavity mode. *Nat. Commun.* **6,** (2015).

4. George, J., Shalabney, A., Hutchison, J. A., Genet, C. & Ebbesen, T. W. Liquid-phase vibrational strong coupling. *J. Phys. Chem. Lett.* **6,** 1027–1031 (2015).

5. Simpkins, B. S. *et al.* Spanning Strong to Weak Normal Mode Coupling between Vibrational and Fabry − Pe´rot Cavity Modes through Tuning of Vibrational Absorption Strength. *ACS Photonics* **2,** 1460 (2015).

6. Yuen-Zhou, J., Saikin, S. K. & Menon, V. M. Molecular Emission near Metal Interfaces: The Polaritonic Regime. *J. Phys. Chem. Lett.* **9,** 6511–6516 (2018).

7. Dunkelberger, A. D., Davidson, R. B., Ahn, W., Simpkins, B. S. & Owrutsky, J. C. Ultrafast Transmission Modulation and Recovery via Vibrational Strong Coupling. *J. Phys. Chem. A* **122,** 965–971 (2018).

8. Mukamel, S. & Nagata, Y. Quantum field, interference, and entanglement effects in nonlinear optical spectroscopy. in *Procedia Chemistry* **3,** 132–151 (2011).

9. De Martini, F., M. Marrocco, and D. M. Transverse Quantum Correlations in the Active Microscopic Cavity. *Phys. Rev. Lett.* **65,** 1853 (1990).

10. Zhong, X. *et al.* Energy Transfer between Spatially Separated Entangled Molecules. *Angew. Chemie - Int. Ed.* **56,** 9034–9038 (2017).

11. Ribeiro, R. F. *et al.* Theory for Nonlinear Spectroscopy of Vibrational Polaritons. *J. Phys. Chem. Lett.* **9,** 3766–3771 (2018).

12. Hutchison, J. A., Schwartz, T., Genet, C., Devaux, E. & Ebbesen, T. W. Modifying chemical landscapes by coupling to vacuum fields. *Angew. Chemie - Int. Ed.* **51,** 1592–1596 (2012).

13. Dunkelberger, A. D., Spann, B. T., Fears, K. P., Simpkins, B. S. & Owrutsky, J. C. Modified relaxation dynamics and coherent energy exchange in coupled vibration-cavity polaritons. *Nat. Commun.* **7,** 13504 (2016).

14. Xiang, B. *et al.* Two-dimensional infrared spectroscopy of vibrational polaritons. *Proc. Natl. Acad. Sci.* **115,** 4845–4850 (2018).

15. Liu, X. *et al.* Strong light-matter coupling in two-dimensional atomic crystals. *Nat. Photonics* **9,** 30–34 (2014).

16. Sun, Z. *et al.* Optical control of roomerature valley polaritons. *Nat. Photonics* **11,** 491–496 (2017).

17. Heylman, K. D., Knapper, K. A. & Goldsmith, R. H. Photothermal microscopy of nonluminescent single particles enabled by optical microresonators. *J. Phys. Chem. Lett.* **5,** 1917–1923 (2014).

18. Ribeiro, R. F., Martínez-Martínez, L. A., Du, M., Campos-Gonzalez-Angulo, J. & Yuen-Zhou, J. Polariton chemistry: controlling molecular dynamics with optical cavities. *Chem. Sci.* (2018). doi:10.1039/c8sc01043a

19. Du, M. *et al.* Theory for polariton-assisted remote energy transfer. *Chem. Sci.* (2018). doi:10.1039/c8sc00171e

20. Tiarks, D., Schmidt-Eberle, S., Stolz, T., Rempe, G. & Dürr, S. A Photon-Photon Quantum Gate Based on Rydberg Interactions. *Nat. Phys.* 1 (2018). doi:arXiv:1807.05795v1

21. Olson, J. *et al.* Quantum Information and Computation for Chemistry. *arXiv* (2017). doi:10.1002/9781118742631

22. Ladd, T. D. *et al.* Quantum computers. *Nature* **464,** 45–53 (2010).

23. Greentree, A. D., Tahan, C., Cole, J. H. & Hollenberg, L. C. L. Quantum phase transitions of light. *Nat. Phys.* **2,** 856–861 (2006).

24. Wang, H., Gu, X., Liu, Y. X., Miranowicz, A. & Nori, F. Tunable photon blockade in a hybrid system consisting of an optomechanical device coupled to a two-level system. *Phys. Rev. A - At. Mol. Opt. Phys.* **92,** 033806 (2015).

25. Rebić, S., Tan, S. M., Parkins, A. S. & Walls, D. F. Large Kerr nonlinearity with a single atom. *J. Opt. B Quantum Semiclassical Opt.* **1,** 490–495 (1999).

26. Birnbaum, K. M. *et al.* Photon blockade in an optical cavity with one trapped atom. *Nature* **436,** 87–90 (2005).

27. Rabl, P. Photon blockade effect in optomechanical systems. *Phys. Rev. Lett.* **107,** (2011).

28. Imamoglu, A., Schmidt, H., Woods, G. & Deutsch, M. Strongly interacting photons in a nonlinear cavity. *Phys. Rev. Lett.* **79,** 1467–1470 (1997).

29. Liang, Q. Y. *et al.* Observation of three-photon bound States in a quantum nonlinear medium. *Science (80-.).* **359,** 783–786 (2018).

30. Chang, D. E., Vuletić, V. & Lukin, M. D. Quantum nonlinear optics - Photon by photon. *Nat. Photonics* **8,** 685–694 (2014).

31. Kiefer, L. M. & Kubarych, K. J. NOESY-Like 2D-IR Spectroscopy Reveals Non-Gaussian Dynamics. *J. Phys. Chem. Lett.* **7,** 3819–3824 (2016).

32. Fournier, J. A., Carpenter, W., De Marco, L. & Tokmakoff, A. Interplay of Ion-Water and Water-Water Interactions within the Hydration Shells of Nitrate and Carbonate Directly Probed with 2D IR Spectroscopy. *J. Am. Chem. Soc.* **138,** 9634–9645 (2016).

33. Saurabh, P. & Mukamel, S. Two-dimensional infrared spectroscopy of vibrational polaritons of molecules in an optical cavity. *J. Chem. Phys.* **144,** 124115 (2016).

34. Hamm, P. & Zanni, M. *Concepts and methods of 2D infrared spectroscopy*. *Concepts and Methods of 2D Infrared Spectroscopy* **9781107000,** (2011).

35. Porter, T. M. *et al.* Direct observation of the intermediate in an ultrafast isomerization. *Chem. Sci.* (2018). doi:10.1039/C8SC03258K

36. Buchanan, L. E. & Xiong, W. in *Encyclopedia of Modern Optics* **2,** 164–183 (2018).

37. Houdré, R., Stanley, R. P. & Ilegems, M. Vacuum-field Rabi splitting in the presence of inhomogeneous broadening: Resolution of a homogeneous linewidth in an inhomogeneously broadened system. *Phys. Rev. A* **53,** 2711–2715 (1996).

38. Khitrova, G., Gibbs, H. M., Jahnke, F., Kira, M. & Koch, S. W. Nonlinear optics of normal-mode-coupling semiconductor microcavities. *Rev. Mod. Phys.* **71,** 1591–1639 (1999).

39. Fehrenbach, G. W., Schäfer, W., Treusch, J. & Ulbrich, R. G. Transient optical spectra of a dense exciton gas in a direct-gap semiconductor. *Phys. Rev. Lett.* **49,** 1281–1284 (1982).

40. Wang, H. *et al.* Transient nonlinear optical response from excitation induced dephasing in GaAs. *Phys. Rev. Lett.* **71,** 1261–1264 (1993).

41. Jahnke, F. *et al.* Excitonic nonlinearities of semiconductor microcavities in the nonperturbative regime. *Phys. Rev. Lett.* **77,** 5257–5260 (1996).

42. Letokhov, V. S. *Principles of nonlinear optical spectroscopy*. *Physics-Uspekhi* **41,** (1998).

43. Zhu, D., Li, C., Zeng, X. & Jiang, H. Tunable-focus microlens arrays on curved surfaces. *Appl. Phys. Lett.* **96,** (2010).

44. Zhu, D., Zeng, X., Li, C. & Jiang, H. Focus-tunable microlens arrays fabricated on spherical surfaces. *J. Microelectromechanical Syst.* **20,** 389–395 (2011).

45. Zhu, D., Lo, C. W., Li, C. & Jiang, H. Hydrogel-based tunable-focus liquid microlens array with fast response time. *J. Microelectromechanical Syst.* **21,** 1146–1155 (2012).

46. Thomas, A. *et al.* Ground-State Chemical Reactivity under Vibrational Coupling to the Vacuum Electromagnetic Field. *Angew. Chemie - Int. Ed.* **55,** 11462–11466 (2016).

Manipulating Optical Nonlinearities of Molecular Polaritons by Delocalization

Supporting Information Appendix

S1. 2D IR spectrometer

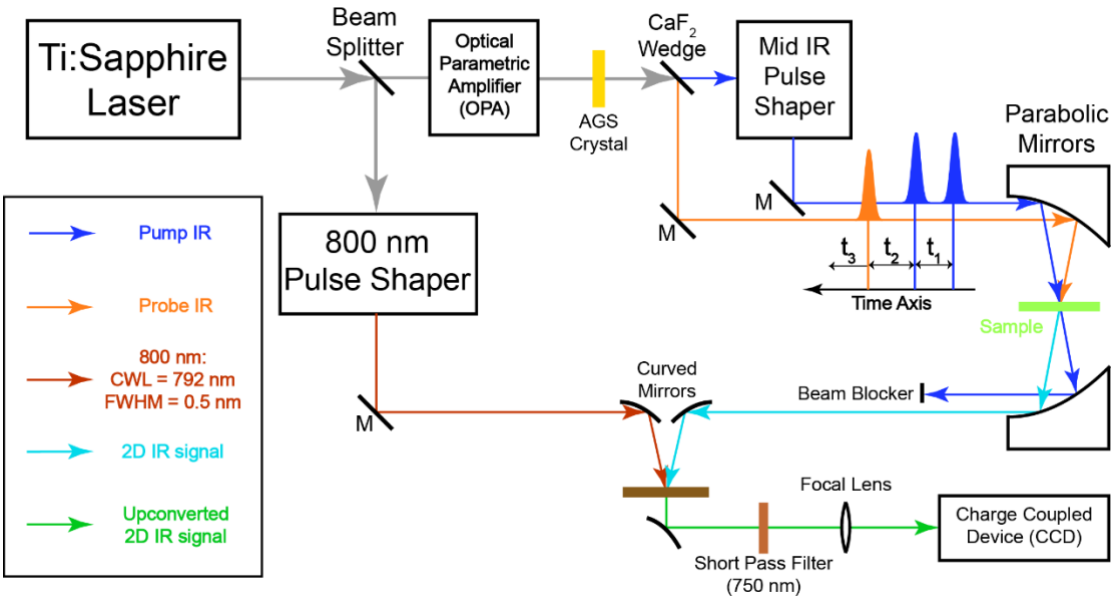

Figure S1. Scheme of two-dimensional infrared experimental setup.

Two-dimensional infrared (2D IR) spectroscopy[1] is applied to investigate the light-matter interaction of a $W(CO)_6$/microcavity system. The setup scheme is shown in Figure S1. 800-nm laser pulses (~35 fs, ~5 W, 1 kHz) generated by an ultrafast Ti:Sapphire regenerative amplifier (Astrella, Coherent) are sent into an optical parametric amplifier (OPA) (TOPAS, LightConversion) which outputs tunable near-IR pulses. The near-IR pulses are converted to mid-IR pulses through a difference frequency generation (DFG) process by a type II $AgGaS_2$ crystal (Eksma). After DFG, a CaF_2 wedge splits the mid IR into two parts: the 95% transmitted part is sent into a Ge-Acoustic Optical Modulator based mid IR pulse shaper (QuickShape, PhaseTech)[2] and is shaped to double pulses, which forms the pump beam arm; the 5% reflected is the probe beam. Both pump (~ 1.1 μJ) and probe (~ 0.2 μJ) are focused by a parabolic mirror (f = 10 cm) and overlap spatially at the sample. The output signal is collimated by another parabolic mirror (f = 10 cm) at a symmetric position and is upconverted to an 800-nm beam at a 5%Mg: $LiNbO_3$ crystal. The 800-nm beam that comes out of the OPA passes through an 800-nm pulse shaper which narrows its spectrum in the frequency domain (center wavelength of 791 nm and a FWHM of 0.5 nm or 9.5 cm^{-1}).

The pulse sequence is shown in Figure S1. Two pump pulses and a probe pulse interact with samples at delayed times (t_1, t_2 and t_3). After the first IR pulse, a vibrational coherence is generated, which is converted into a population state by the second IR pulse and is characterized by scanning t_1 (0 to 6000 fs with 20 fs steps) using the mid IR pulse shaper. A rotating frame at f_0 = 1583 cm^{-1} is applied to shift the oscillation period to 80 fs and to make the scanning step meet the Nyquist frequency requirement. After waiting for t_2, the second coherence is generated by the third IR pulse (probe), which forms a macroscopic polarization that subsequently emits an IR signal. This IR signal is upconverted by a narrow-band 800 nm beam. The upconversion process covers the t_3 time delay and the 800-nm pulse duration (full width at half maximum = 0.5 nm) determines the scanning length of t_3. The monochromator and CCD (Andor) experimentally Fourier transform the

upconverted signal, thus generating a spectrum along the ω_3 axis. Numerical Fourier transform along the t_1 axis is required to plot the first coherence along ω_1. The resulting 2D IR spectra are plotted against ω_1 and ω_3. The t_2 time delay is scanned by a computerized delay stage which is controlled by home-written LabVIEW programs to characterize the dynamic features of the system. A rotational stage is mounted on the sample stage to control the tilt angle and, therefore, the wavevector space. One special requirement for this experiment is that the rotation axis of the rotational stage needs to be parallel to the incidence plane formed by the pump and probe beams. In this way, we ensure that the in-plane wavevectors, $k_{||}$, of pump and probe pulses are the same. The $k_{||}$ value the of pump and probe beams are determined by checking the 1D transmission polariton spectra of the pump and probe pulses before and after 2D IR acquisitions.

S2. Sample preparation

The $W(CO)_6$ (Sigma-Aldrich) /cavity system is prepared in IR spectral cell (Harrick) containing two dielectric CaF_2 mirrors separated by a 12 or 25 μm spacer and filled with $W(CO)_6$/hexane solution (concentration varies from 5 mM to 50 mM). The dielectric mirror has a ~96% reflectivity. Because the Rabi splitting (20 to 37 cm^{-1}) is larger than the full-width-at-half-max of both cavity (~11 cm^{-1}) and $W(CO)^6$ vibrational (~3 cm^{-1}) modes, the strong coupling criteria is satisfied.

S3. UP/LP Spectral Cuts of 25-micron System at Different t_2

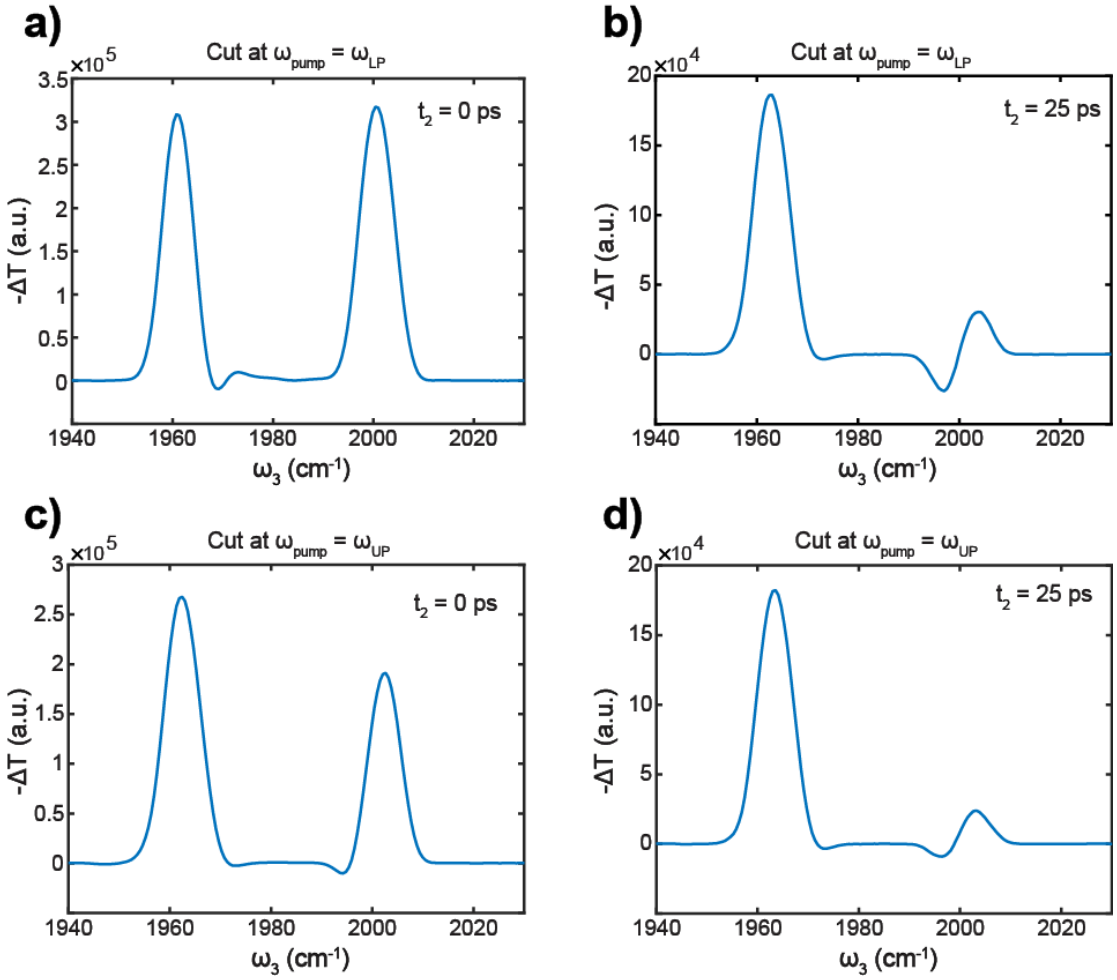

Figure S2 Spectral cuts of 2D IR spectra of 25-micron system at (a) t_2 = 0 ps and ω_{pump} =ω_{LP}; (b) t_2 = 25 ps and ω_{pump} =ω_{LP}; (c) t_2 = 0 ps and ω_{pump} =ω_{UP}; (d) t_2 = 25 ps and ω_{pump} =ω_{UP}, indicating the spectral cuts of 2D IR signal match with pump-probe spectral lineshape, though there is small difference between UP and LP cuts.

S4. 2D IR and Pump-probe Spectra with 12 and 25-micron Systems

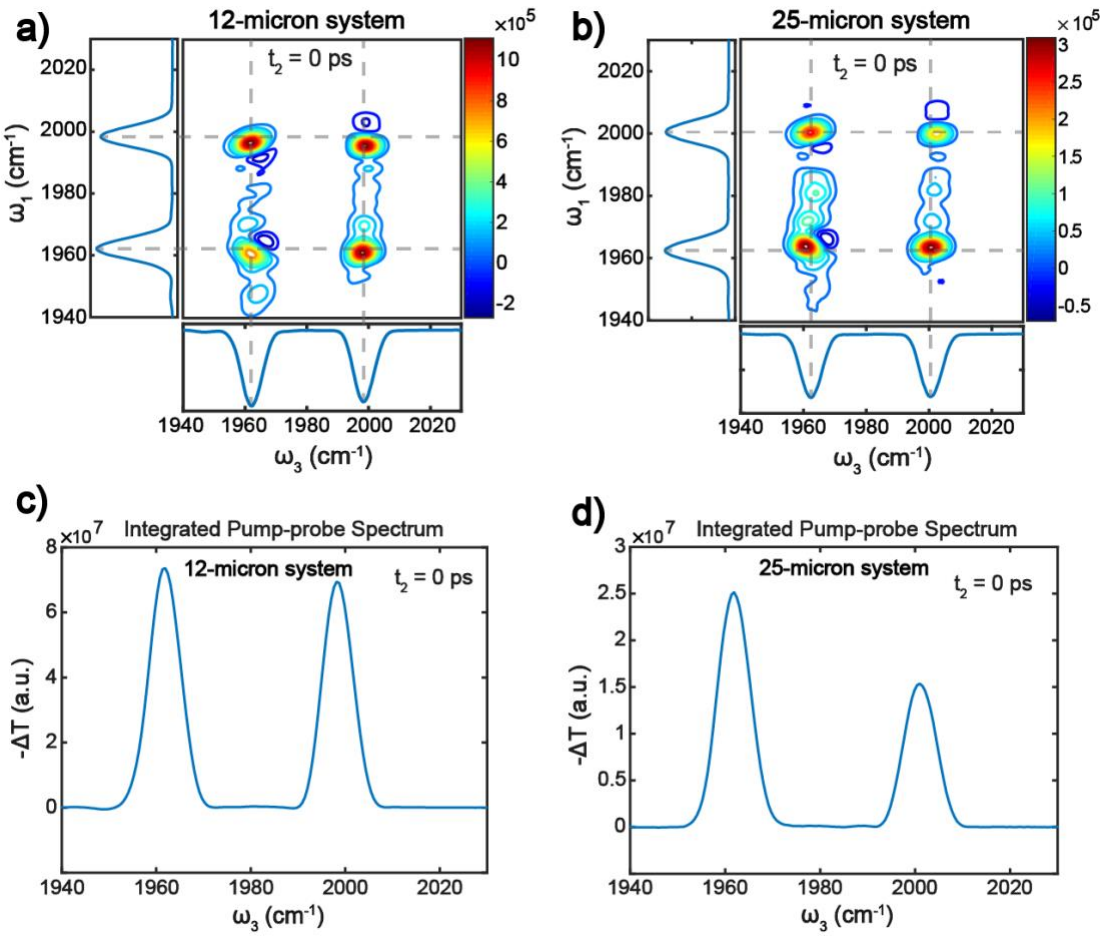

Figure S3. 2D IR spectra of (a)12-micron system and (b) 25-micron system; Integrated pump-probe spectra of (c)12-micron system and (d) 25-micron system. Note that the color bars of (a) and (b) indicate that 12-micron system has larger nonlinearity than 25-micron system

S5. 2D IR Spectra at Various Molecular Concentrations

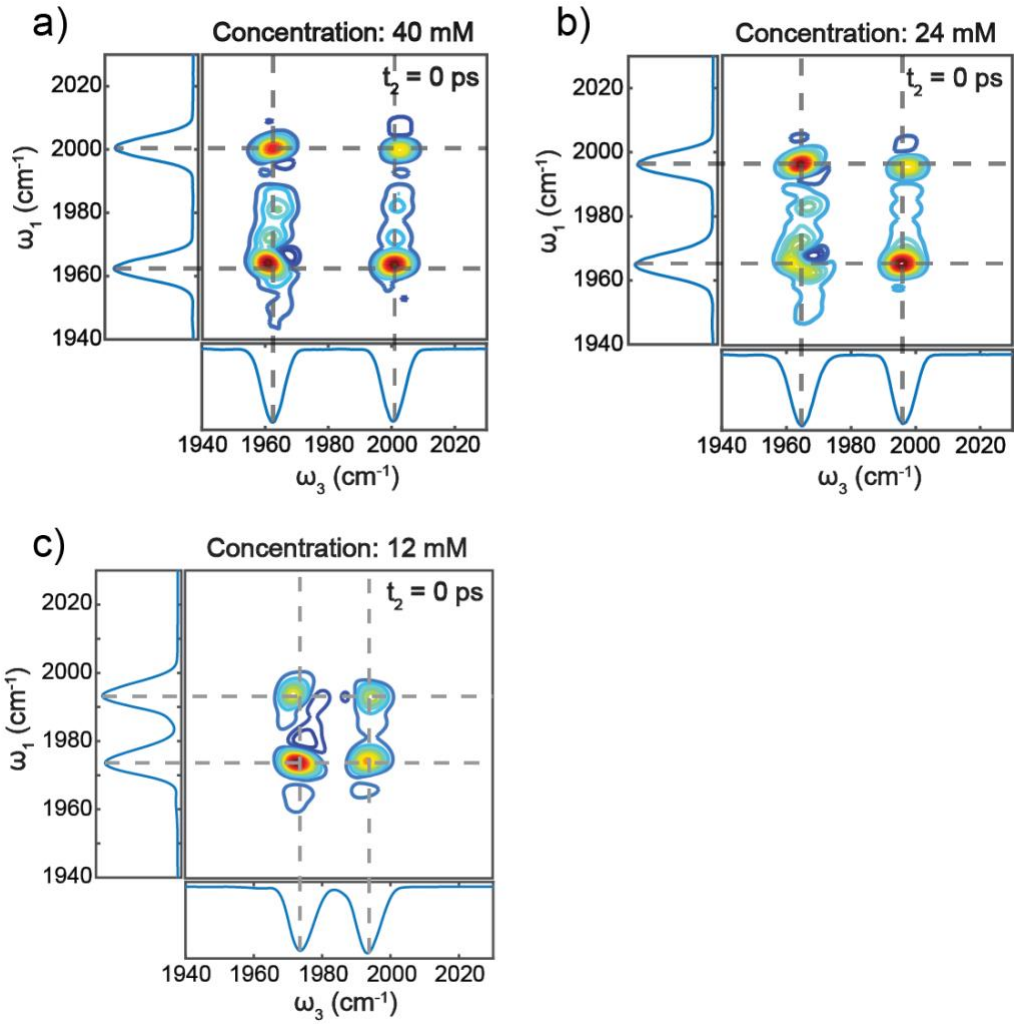

Figure S4. 2D IR spectra of 25-micron system at t_2 = 0 ps with various concentrations: (a) 40 mM; (b) 24 mM; (c) 12 mM.

S6. Three-Dimensional Fourier Transformation

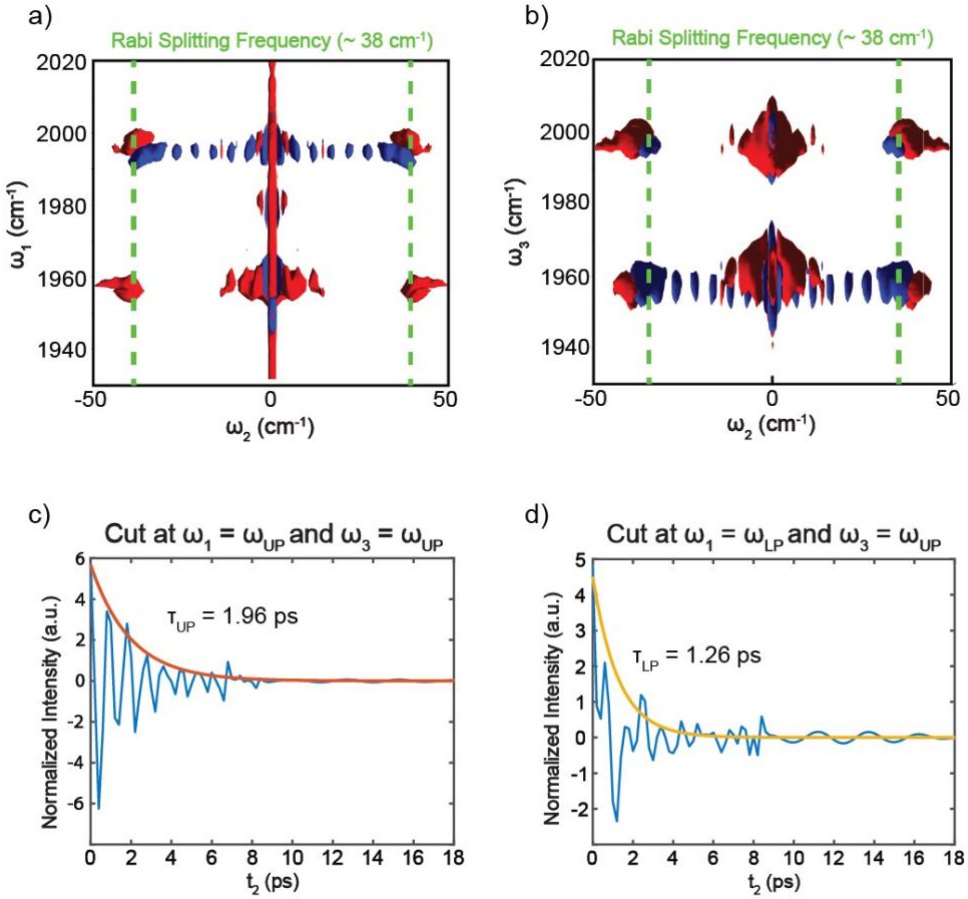

Figure S5. 3D FFT frequency domain (ω_1-ω_2-ω_3) spectra: (a) Viewing from ω_1-ω_2 plane; (b) Viewing from ω_3-ω_2 plane; Dephasing traces of (c) cut at $\omega_1 = \omega_{UP}$ and $\omega_3 = \omega_{UP}$; (d) cut at $\omega_1 = \omega_{LP}$ and $\omega_3 = \omega_{UP}$.

2D-IR spectra at early times (t_2 = 0 ~ 5 ps) show unambiguous oscillating features at UP and LP frequencies (see figure 4a) and their period (0.8 ps) suggests the frequency of the oscillation is close to Rabi splitting frequency (~38 cm^{-1}). This hidden information is a key evidence of the coherence between lower and upper polaritons. To disentangle the oscillating part from the overall 2D signal, 3D Fourier transform is applied to the combined 2D matrices at different time delays. An additional frequency axis (ω_2) is generated from applying FFT to the t_2 axis. From both figures S5 a and b, we can clearly see the features at $|\omega_2|$ = 38 cm^{-1} (referred to as AC part) besides the non-oscillating part at ω_2 ~ 0 cm^{-1} (referred to as DC part). DC and AC parts can be disentangled by applying a filter to the 3D matrix and doing an inverse Fourier transfer to the DC and AC parts.

To further analyze the coherent dynamics, amplitudes of the AC part at at $\omega_1 = \omega_{UP}/\omega_3 = \omega_{UP}$ and $\omega_1 = \omega_{LP}/\omega_3 = \omega_{UP}$ have been extracted and plotted versus t_2 (figures S5 c and d). The UP-UP oscillating trace exhibits nearly perfect dephasing dynamics and can be fitted with a single exponential which gives a lifetime of ~2 ps; the LP-UP trace, on the other hand, deviates from pure dephasing dynamics, likely because the overtone transitions of dark reservoir modes (υ_{12} ~ 1968 cm^{-1} and υ_{23} ~ 1950 cm^{-1}) perturb the LP state.

S7. Feynman Diagrams: Coherence Generations

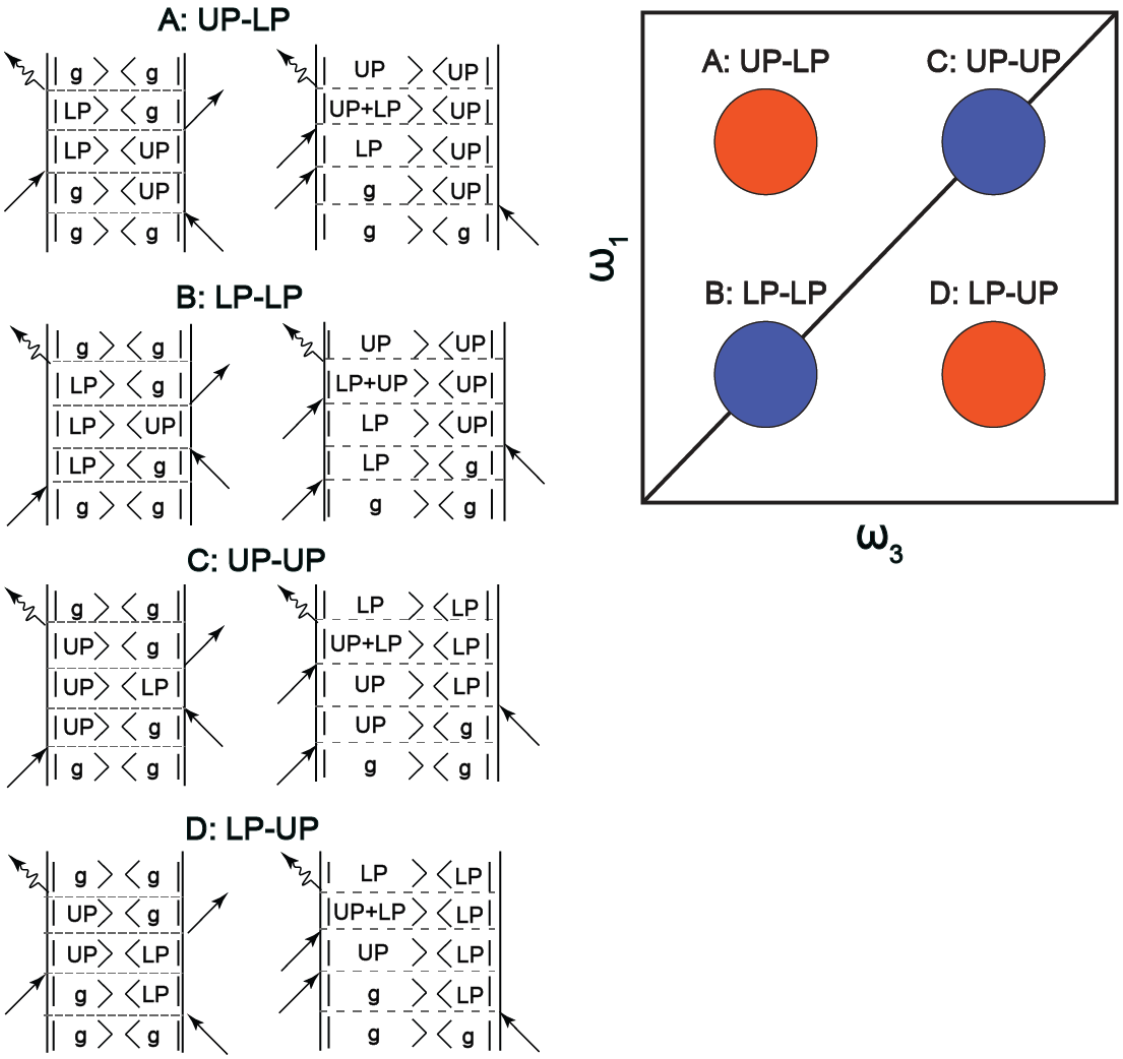

Figure S6. Feynman diagrams representing the oscillating nonlinear responses (AC components) in each region: A) $\omega_1 = \omega_{UP}$ and $\omega_3 = \omega_{LP}$; B) $\omega_1 = \omega_{LP}$ and $\omega_3 = \omega_{LP}$; C) $\omega_1 = \omega_{UP}$ and $\omega_3 = \omega_{UP}$; D) $\omega_1 = \omega_{LP}$ and $\omega_3 = \omega_{UP}$.

S8. Pump-on and Pump-off Spectra with 12 and 25-micron Systems

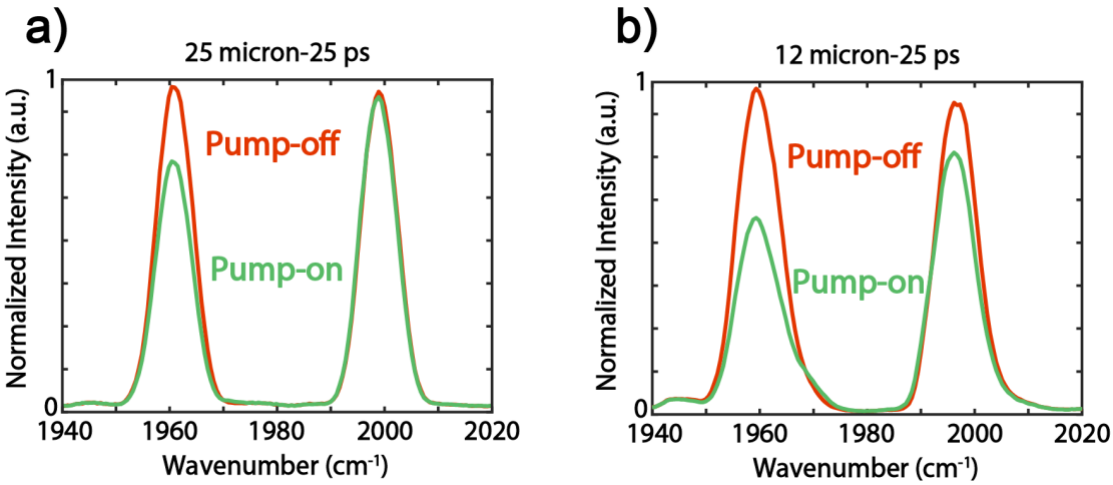

Figure S7. Pump-on and pump-off spectra at t_2 = 25 ps with cavity longitudinal lengths of (a) 25 μm; (b) 12 μm.

S9. Early-time Dynamics of 2D IR Spectral Cuts at LP and Dark States

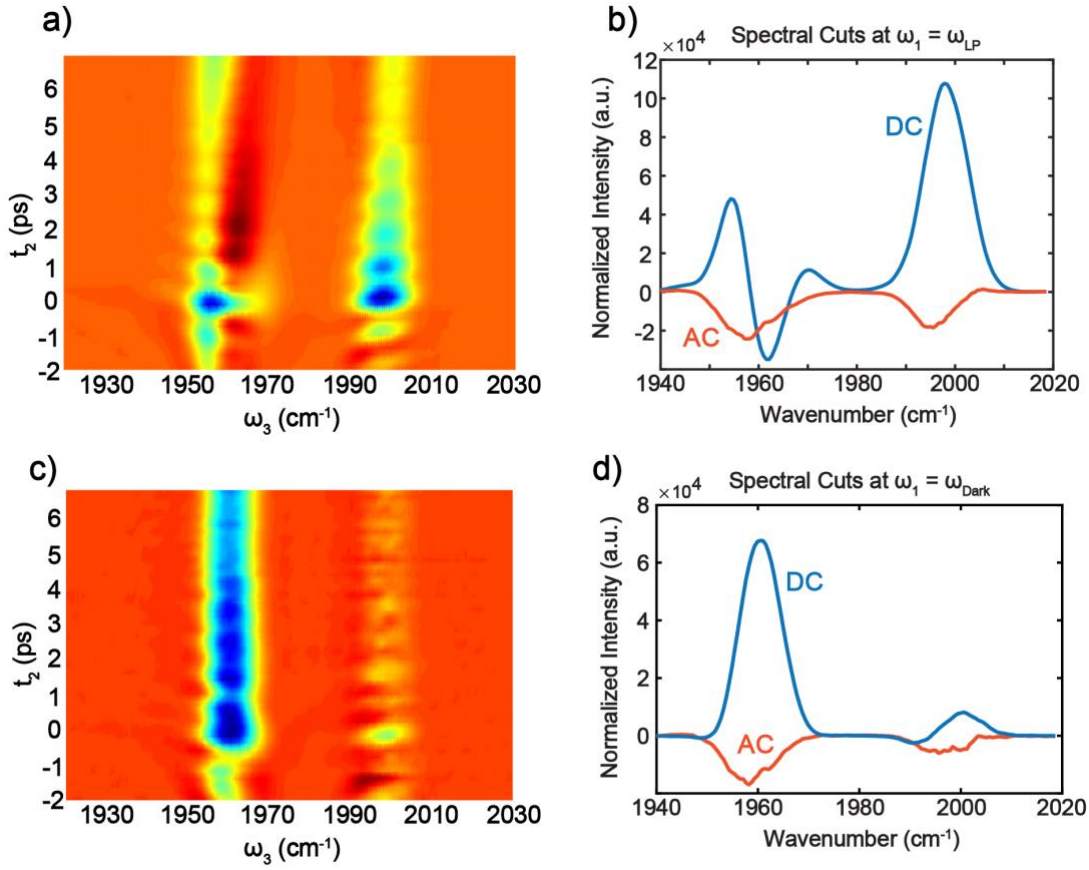

Figure S8. Early-time dynamics of 2D IR spectral cut at (a) $\omega_1=\omega_{LP}$ and (c) $\omega_1=\omega_{Dark}$ between -2 to 7 ps. AC and DC spectral cuts at (b) $\omega_1=\omega_{LP}$, and (d) $\omega_1=\omega_{Dark}$ at t_2=0.8 ps.

Figure S8 a and c show the t_2 dynamics of spectral cuts at $\omega_1=\omega_{LP}$ and $\omega_1=\omega_{Dark}$, respectively. Compared to the dynamics of UP-cut (figure 3a), LP-cut signal has significant DC component though the oscillation feature is still obvious. 3D-FFT has been performed and AC and DC components of LP-cuts at t_2 = 0.8 ps have been obtained. From figure S8b, it is clear that the DC component contributes more compared to the AC signal due to polaritonic coherent states. The strong DC signal could be due to the strong features in the LP spectral cut which is strongly perturbed by overtone transitions of $W(CO)_6$ dark modes (v_{12} ~ 1968 cm^{-1} and v_{23} ~ 1950 cm^{-1}) even at early-times. When the pump frequency equals that of the dark mode, the signal is mainly non-oscillating (figure S8c). After Fourier filtering, it does show an AC component, which is most likely due to spectral overlap with the oscillating polariton spectral features (figure S8d). As discussed in the main text, |LP><UP| and |UP><LP| coherence states are the only sources for Rabi oscillations (AC part). Due to spectral congestion and overlaps, the tail of AC component of LP and UP peaks also causes dark mode spectral features to “oscillate” weakly. Nevertheless, as clearly shown in the 3D IR plot (Fig.S5), the Rabi oscillation peaks near ω_2=38 cm^{-1}, only show up at LP and UP transitions, but not at dark modes, which provide the best evidence that dark modes do not involve in Rabi oscillation. Still, the weakness of oscillations in the dark mode dynamics and its contamination by the LP make the UP spectral cuts the cleanest for analysis of the pure polaritonic response, which is shown in the main text.

S10. Classical Simulation of Nonlinearity of Polariton Systems

The transmission intensity of the coupled cavity can be expressed as[3–5]

$$T_c = \frac{T^2 e^{-\alpha L}}{1+R^2 e^{-2\alpha L}-2Re^{-\alpha L}cos(4\pi nL\nu+2\varphi)}. \quad (1)$$

In equation (1), R and T are the reflectance and transmittance of the FP cavity mirrors around 1983 cm^{-1}, which were set to be 96% and 4%. α is the absorption coefficient, L is the cavity longitudinal length, n is the real part of the cavity mirror complex refractive index and φ is the phase shift. α, the absorption coefficient, is equal to $1 + 4\pi k\nu$, where k is the imaginary part of the complex refractive index and ν is the frequency ranging from 1940 to 2030 cm^{-1}. As mentioned in the main text, by changing the homogeneous linewidth of fundamental mode of $W(CO)_6$, (Γ_1), the refractive index (n, k) is modulated accordingly, (see Eqs. (2) ~ (5)[4]). This effect causes variation of the transmission intensity (T_c), and in particular a larger molecular homogeneous linewidth implies enhanced polariton broadening. Another parameter that is related to the molecular vibrations is A_1, the intensity of the oscillator, which is proportional to the density of molecular vibrations. Adjusting A_1 does not lead to the purely adsorptive polariton bleach feature, instead, it causes polariton resonance shifts in frequency, i.e. Rabi splitting contraction. Thus, the semiclassical simulation results indicate that changes of Γ_1, but not A_1, could cause polariton bleach features. We define

$$n(\nu) = \sqrt{\frac{\varepsilon_1+\sqrt{\varepsilon_1^2+\varepsilon_2^2}}{2}} \quad (2)$$

$$k(\nu) = \sqrt{\frac{-\varepsilon_1+\sqrt{\varepsilon_1^2+\varepsilon_2^2}}{2}} \quad (3)$$

where ε_1 and ε_2 are the real and imaginary parts of dielectric constant, expressed as

$$\varepsilon_1 = \varepsilon_{inf} + \sum_{i=1}^{3}\left[\frac{A_i(\nu_i^2-\nu^2)}{(\nu_i^2-\nu^2)^2+(\Gamma_i\nu)^2}\right] \quad (4)$$

$$\varepsilon_2 = \sum_{i=1}^{3}\left[\frac{A_i\Gamma_i\nu}{(\nu_i^2-\nu^2)^2+(\Gamma_i\nu)^2}\right] \quad (5)$$

where ν_{0i} are the frequencies of vibrational transitions 0->1 (1983 cm^{-1}), 1->2 (1968 cm^{-1}) and 2->3 (1953 cm^{-1}) of $W(CO)_6$, and the Γ_i are the width of the corresponding vibrational modes. A_i are the amplitudes, and A_1 is set to be a large number while A_2 and A_3 are insignificant compared to A_1, since the fundamental mode has the largest population and is in resonance with the cavity photon.

S11. Comparison of LP/UP Cuts of Both 12-μm and 25-μm Systems

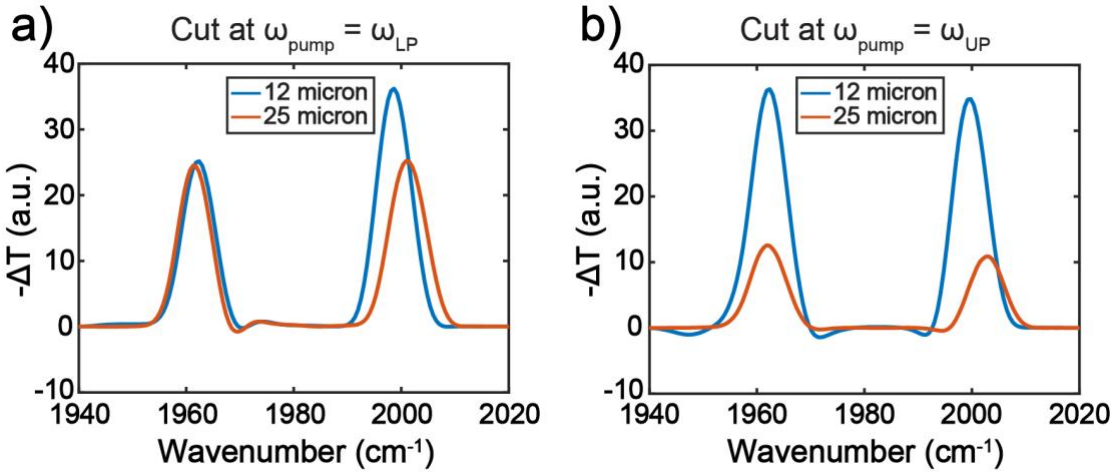

Figure S9. 2D IR Spectral cuts of both 12-μm and 25-μm systems for comparison at (a) $\omega_1=\omega_{LP}$; (b) $\omega_1=\omega_{UP}$. t_2 = 0 ps

S12. Two-component Spectral Fitting of Absorptive Pump-probe Spectra

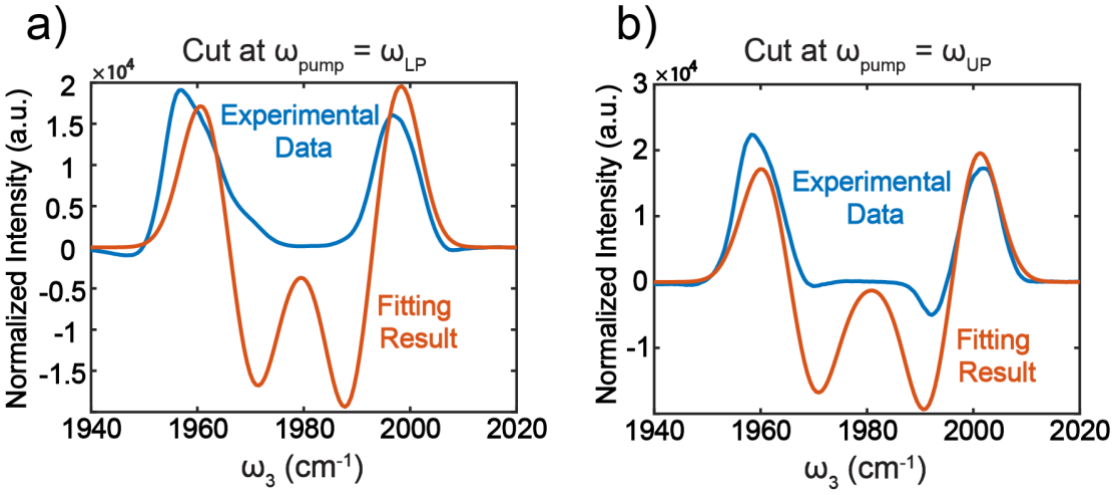

Figure S10. Spectral fitting of 25-μm systems with t_2 = 0 ps at (a) $\omega_1=\omega_{LP}$; (b) $\omega_1=\omega_{UP}$. The fitting model is composed of an absorptive feature on the LP-side (dark mode overtone responses) and the derivative shape at the LP/UP frequencies (due to Rabi splitting contraction). The results indicate that dark mode overtone responses together with Rabi splitting contraction are not enough to reproduce the experimental features.

Two-component spectral fitting was applied to the LP/UP spectral cuts of 2D-IR spectrum of 25-μm system at t_2 = 0 ps, using the following equation

$$Spec_{fit} = \underbrace{\left\{\alpha_1\left[a_0 e^{-\left(\frac{x-b_0}{c_0}\right)^2}\right]\right\}}_{(1)} + \underbrace{\left\{\alpha_2 \sum_{i=1}^{2}\left[a_i e^{-\left(\frac{x-b_i}{c_i}\right)^2} - a_i e^{-\left(\frac{x-b_i+\Delta x}{c_i}\right)^2}\right]\right\}}_{(2)}. \quad (6)$$

In the equation, terms (1) and (2) represent spectral components of the dark mode overtone response and the Rabi splitting contraction, respectively, as shown in our previous works; x is the frequency and a, b and c are the amplitude, peak position and

width of a Gaussian peak; Δx is the amount of peak-shift and α_1 and α_2 are the coefficients which modulate the compositions of the two components.
From figures S10 a and b, it is clear that the spectral cuts from the experimental data cannot be fitted with only the two components mentioned in equation (6). Hence, an additional component that represents the polariton-bleach type of signal is needed.

S13. Cavity Coherence Volume Calculation

The cavity coherence volume can be calculated based on the following equation[6]

$$V_{\text{eff}} = S_{\text{eff}} \cdot l = \frac{\pi l^2 \lambda_v}{1-R} \quad (7)$$

where V_{eff} and S_{eff} are the effective volume and area of a specific cavity mode, l is the cavity longitudinal length (12 and 25 μm), λ_v is the wavelength of vibrational transition (5042.86 nm in our case, corresponding to 1983 cm^{-1}) and R is the reflectivity of the DBRs which is 96% in the experiments.
The resulting coherence volumes of the 12 and 25-μm systems are 2.5×10^5 and 0.57×10^5 μm^3, respectively, i.e., the cavity with longest length has a coherence volume that is four times greater than that with the shortest.

S14. Dependence of Polariton Nonlinearities on Cavity Length

A. Polariton-polariton nonlinearities from molecular anharmonicity

Although the microscopic mechanism of the polariton bleach effect is not entirely clear yet, we show in this section that when dark modes are disregarded, the dominant coherent polariton nonlinear interactions induced by quartic couplings (most relevant at low energies for homogeneous and isotropic systems like the molecular solution studied here) can lead to inverse scaling with respect to the cavity length due to polariton delocalization. The discussion in this section is limited to polariton-polariton interactions relevant at short times relative to their decay. In the next section, we employ the results obtained in Ref. [7] to comment on the cavity length dependence of the pump-probe response in the case where polaritons have decayed and the transient state of the system can be well-approximated by an incoherent population of bare molecule excited-states[7].

Let a planar infrared cavity consisting of two metal mirrors with surface area S separated by longitudinal length L_z host N molecules homogeneously distributed across the volume $V = SL_z$. The TE and TM modes of the cavity electromagnetic field are obtained by using periodic boundary conditions for the electromagnetic field along the x and y directions and metal-dielectric interface boundary conditions from Maxwell equations. For the sake of simplicity, we retain for what follows only a single TE cavity photon band with modes parametrized by $\mathbf{k} = (k_x, k_y)$ having resonance frequency $\omega(\mathbf{k})$[8]. The vibrational frequency and position of the molecule i in the set $\{1,\ldots,N\}$ are given by ω_i and $\mathbf{r}_i = (x_i, y_i, z_i)$, respectively. The light-matter interaction is treated within the dipole approximation in the rotating-wave-approximation (only excitation-number conserving terms are included)[8]. In the absence of anharmonicity, the Hamiltonian of the hybrid system is given by:

$$H_0 = \sum_{i=1}^{N} \hbar\omega_i a_i^\dagger a_i + \sum_{\mathbf{k}} \hbar\omega(\mathbf{k}) b^\dagger(\mathbf{k}) b(\mathbf{k}) + \sum_{i=1}^{N}\sum_{\mathbf{k}} \left[\bar{g}_{i\mathbf{k}} a_i^\dagger b(\mathbf{k}) + g_{i\mathbf{k}} b^\dagger(\mathbf{k}) a_i\right] \tag{8}$$

where a_i and $b(\mathbf{k})$ are the molecular and photonic annihilation operators, g_{ik} is the coupling constant between molecule i and cavity mode $\mathbf{k}$ and $\overline{g_{ik}}$ is its complex conjugate. The detailed form of g_{ik} can be found elsewhere. For our purposes, all that is relevant is that

$$g_{i\mathbf{k}} \propto e^{-i\mathbf{k}\cdot\mathbf{r}_i}\sqrt{\omega_{\mathbf{k}}} \tag{9}$$

where $\mathbf{k} \cdot \mathbf{r}_i = (k_x, k_y) \cdot (x_i, y_i)$[9]. Disregarding inhomogeneous broadening of the molecular vibrations (i.e., suppose all molecular frequencies are ω_0), the polariton modes of this Hamiltonian become obvious by performing a canonical transformation of the local molecular operators into a collective basis adapted to the form of the light-matter interaction given above[10]. Specifically, the following *bright* molecular operators are defined:

$$a(\mathbf{k}) = \sum_{i=1}^{N} \frac{g_{i\mathbf{k}}}{g_{\mathbf{k}}} a_i, \quad g_{\mathbf{k}} = \sqrt{\sum_{i=1}^{N} |g_{i\mathbf{k}}|^2} \propto \sqrt{N} \tag{10}$$

There exists also $N_d = N - N_k$ dark modes (where $N_k \propto S$ is the number of cavity photon modes included in our description) which form the complement to the bright operators $a(\mathbf{k})$ in the space of annihilation operators[10]. In the collective basis, the quadratic part of the Hamiltonian is written as:

$$H_0 = \hbar\omega_0 \sum_{\mathbf{k}} a^\dagger(\mathbf{k}) a(\mathbf{k}) + \sum_{\mathbf{k}} \hbar\omega(\mathbf{k}) b^\dagger(\mathbf{k}) b(\mathbf{k}) + \sum_{\mathbf{k}} \left[\bar{g}_{\mathbf{k}} a^\dagger(\mathbf{k}) b(\mathbf{k}) + g_{\mathbf{k}} b^\dagger(\mathbf{k}) a(\mathbf{k})\right] + \hbar\omega_0 \sum_{d=1}^{N_d} \alpha_d^\dagger \alpha_d \tag{11}$$

where the operators α_d are the annihilation operators of dark modes. The bright normal modes of the above Hamiltonian are given by the lower (LP) and upper polaritons (UP) with annihilation operators written as[10]:

$$\alpha_{\mathrm{LP}}(\mathbf{k}) = \cos(\theta_{\mathbf{k}}/2) a(\mathbf{k}) + \sin(\theta_{\mathbf{k}}/2) b(\mathbf{k}), \tag{12}$$

$$\alpha_{\mathrm{UP}}(\mathbf{k}) = -\sin(\theta_{\mathbf{k}}/2) a(\mathbf{k}) + \cos(\theta_{\mathbf{k}}/2) b(\mathbf{k}) \tag{13}$$

where the specific form of the mixing angles $\theta_{\mathbf{k}}$ and polariton frequencies $\omega_{\mathrm{LP}}(\mathbf{k})$ and $\omega_{\mathrm{UP}}(\mathbf{k})$ are inessential for our discussion.

In order to describe polariton nonlinearities we need to introduce molecular anharmonicity to the hybrid cavity Hamiltonian. At low energies (i.e., when only the first few excited-states are probed) only cubic and quartic nonlinearities are relevant[11]. Retaining only those interactions that preserve the excitation number and disregarding nonlocal interactions, the nonlinear part of the Hamiltonian can be written generically as[7]:

$$H_{\mathrm{I}} = \Delta \sum_{i=1}^{N} a_i^{\dagger} a_i^{\dagger} a_i a_i + \eta \sum_{i\mathbf{k}} \left[g_{i\mathbf{k}} a_i^{\dagger} a_i^{\dagger} a_i b(\mathbf{k}) + b^{\dagger}(\mathbf{k}) a_i^{\dagger} a_i a_i \right] \tag{14}$$

where Δ parametrizes the mechanical anharmonicity (deviation from harmonic energy spectrum of a single vibration), η quantifies deviations of the ith molecule vibrational transition dipole function from linearity with respect to displacement. In the hybrid cavity normal mode basis, H_{I} can be written as a sum of polariton-polariton, polariton-dark, and dark-dark interactions. The polariton-polariton interactions take the following form:

$$H_{\mathrm{I}}^{\text{pol-pol}} = \sum_{p_1 p_2 p_3 p_4}^{\mathrm{LP,UP}} \sum_{\mathbf{k}_1 \mathbf{k}_2 \mathbf{k}_3 \mathbf{k}_4} V_{p_1 p_2, p_3 p_4}^{\mathrm{L}}(\mathbf{k}_1, \mathbf{k}_2, \mathbf{k}_3, \mathbf{k}_4) \alpha_{p_1}^{\dagger}(\mathbf{k}_1) \alpha_{p_2}^{\dagger}(\mathbf{k}_2) \alpha_{p_3}(\mathbf{k}_3) \alpha_{p_4}(\mathbf{k}_4) \tag{15}$$

where the p_i's correspond to either LP or UP and $V_{p_1 p_2 p_3 p_4}^{L}(\boldsymbol{k}_1, \boldsymbol{k}_2, \boldsymbol{k}_3, \boldsymbol{k}_4)$ are the coupling constants for the corresponding polariton-polariton interactions. The coupling arising from mechanical anharmonicity satisfies the following relations:

$$\begin{aligned} V_{p_1 p_2, p_3 p_4}^{\Delta}(\mathbf{k}_1, \mathbf{k}_2, \mathbf{k}_3, \mathbf{k}_4) &\propto \Delta \sum_{i=1}^{N} \frac{\bar{g}_{i\mathbf{k}_1}}{g_{\mathbf{k}_1}} \frac{\bar{g}_{i\mathbf{k}_2}}{g_{\mathbf{k}_2}} \frac{g_{i\mathbf{k}_3}}{g_{\mathbf{k}_3}} \frac{g_{i\mathbf{k}_4}}{g_{\mathbf{k}_4}} \\ &\propto \Delta \sum_{i=1}^{N} \frac{e^{-i(\mathbf{k}_1 + \mathbf{k}_2 - \mathbf{k}_3 - \mathbf{k}_4) \cdot \mathbf{r}_i}}{N^2} \\ &\approx c_{\Delta} \frac{\Delta}{N} \delta_{\mathbf{k}_1 + \mathbf{k}_2 - \mathbf{k}_3 - \mathbf{k}_4} \end{aligned} \tag{16}$$

where $\delta_{\mathbf{q}}$ is the discrete delta function and c_{Δ} is a constant independent of particle number (in the thermodynamic limit). To obtain the last expression we used that the number of molecules is macroscopic, and these are distributed randomly inside the cavity so that the dominant contribution to the polariton-polariton interaction preserves the in-plane wave-vector. For the electrical anharmonicity term we find a similar result:

$$V_{p_1 p_2, p_3 p_4}^{\eta}(\mathbf{k}_1, \mathbf{k}_2, \mathbf{k}_3, \mathbf{k}_4) \approx \frac{\eta(\mathbf{k}_1 + \mathbf{k}_2 - \mathbf{k}_3)}{N} \delta_{\mathbf{k}_1 + \mathbf{k}_2 - \mathbf{k}_3 - \mathbf{k}_4} \tag{17}$$

where $\eta(\mathbf{k}_1 + \mathbf{k}_2 - \mathbf{k}_3)$ is a density-dependent coupling constant of the order of the Rabi splitting.

Further simplification arises from noting that the experimental nonlinear response is measured at $\mathbf{k} \approx 0$, and therefore the dominant contributions will have all $\mathbf{k}_i$ close to zero.). Taking for simplicity only the interaction terms with constant wave-vector the nonlinear response can be expressed as $\sum_{\boldsymbol{k}} F(\boldsymbol{k})/N$, where $F(\boldsymbol{k})$ is independent of particle number. In the continuum limit of the photonic system, it follows that $\sum_{\boldsymbol{k}} F(\boldsymbol{k}) = (2\pi)^{-2} S \int d\boldsymbol{k}$ F($\mathbf{k}$). Writing $N = \rho S L_z$ where ρ is the molecular density, we find that under the discussed assumptions the nonlinear polariton-polariton coupling constant is inversely proportional to ρL_z which therefore implies that for a fixed molecular density, increasing the cavity length

leads to an inversely proportional reduction in the dominant nonlinear polariton-polariton couplings. Noticeably, *this property is a byproduct of the polariton delocalization across the molecular ensemble*. However, both electrical and mechanical anharmonicity also give rise to shifts in the polariton energies[1,7], so the interactions discussed above cannot cause the polariton bleach effect observed at short pump-probe times. It is likely that nonlinear polariton-polariton scattering is too weak for the system studied, and an alternative mechanism generates the enhanced broadening giving rise to the polariton bleach effect.

B. Long probe-delay regime

In the case where the probe delay time is much longer than the polariton lifetimes, the situation is different than that discussed above. As shown in Refs. [1, 7], the pump-probe transmission can be reasonably approximated by an analytical expression obtained by assuming the pump-induced transient state of the system contains an incoherent molecular population in the first excited-state. In this section, we employ these results to show that the inverse scaling with respect to cavity length also appears in a description of the long-time delay regime of the pump-probe measurements. This model differs from that explored in the previous section as it includes only an effective single cavity photon, so the spatial dispersion of the field is entirely disregarded.

In the notation of Ref. [7], the following equation gives the relative differential pump-probe transmission when the fraction of molecular excited-states f_{pu} in the cavity photon volume is small enough

$$\frac{\Delta T^{\mathrm{pp}}(\omega')}{T^{(1)}(\omega')} = f_{\mathrm{pu}}\Omega_R^2 \mathrm{Re}\left[\frac{-2\Delta + 2\delta\left[\omega' - \omega_0 + i(\gamma_3+\gamma_1)/2\right] + \delta^2(\omega' - \omega_0 + i\gamma_1)}{[\omega' - (\omega_0 - 2\Delta) + i\gamma_3](\omega' - \omega_{\mathrm{LP}} + i\gamma_{\mathrm{LP}}/2)(\omega' - \omega_{\mathrm{UP}} + i\gamma_{\mathrm{UP}}/2)}\right], \quad (18)$$

where $\delta(\Delta)$ parametrizes electrical (mechanical anharmonicity), Ω_R is the Rabi splitting directly proportional to the number of molecules N_{coh} in the coherence volume of the cavity photon, and $T^{(1)}(\omega)$ is the linear response transmission spectrum. Suppose we make the cavity transverse length L significantly longer so that the cavity photons which hybridize with the molecular polarization belong to a different band. For a fixed Rabi splitting, the only parameter in the above expression which is expected to change significantly is f_{pu}[1]. Indeed, linear transmission experiments performed at the cavities with distinct values of L showed no essential difference in the polariton transmission linewidths.

Let $f_{\mathrm{pu}}(x)$ denote the value of f_{pu} for a cavity with longitudinal length x with a given Rabi splitting Ω_R which is fixed for all x, and $V_L = S_{\mathrm{eff}} \times L$ the effective photon mode volume for a cavity with length L. Then,

$$f_{\mathrm{pu}}(L) = \frac{1}{N_{\mathrm{coh}}(L)} \sum_{i \text{ in } V_L} \langle a_i^\dagger a_i \rangle_L = \frac{N_{\mathrm{pu}}(L)}{N_{\mathrm{coh}}(L)} \quad (19)$$

---

[1] Note the cavity photon linewidth is expected to be narrower for a longer cavity due to its longer lifetime, but the linewidth induced by absorption also increases, thus roughly offsetting the narrowing of the cavity mode and making the γ_{LP} and γ_{UP} of cavities with different transverse lengths very similar

where $N_{pu}(L)$ is the mean number of molecules in the excited-state in the coherence volume of the cavity with length L. The molecular density ρ is fixed in the experiments with cavities of different sizes, so we can write N_{coh} (L) = ρV_L. Therefore, the ratio of dark molecular excited population in the cavity with length 2L in comparison to the cavity with length L is given by:

$$\begin{aligned}\frac{f_{\mathrm{pu}}(2L)}{f_{\mathrm{pu}}(L)} &= \frac{\sum_{i \text{ in } V_{2L}} \langle a_i^\dagger a_i \rangle_{2L}}{\sum_{i \text{ in } V_L} \langle a_i^\dagger a_i \rangle_L} \times \frac{V_L}{V_{2L}} \\ &= \frac{\sum_{i \text{ in } V_{2L}} \langle a_i^\dagger a_i \rangle_{2L}}{\sum_{i \text{ in } V_L} \langle a_i^\dagger a_i \rangle_L} \times \frac{S_L}{2S_{2L}}\end{aligned} \tag{20}$$

Recall that $N_{pu}(L)$ is proportional to the total energy absorbed from the pump field (including both polariton and dark mode absorption). It follows that $N_{pu}(2L) \approx 2\, N_{pu}(L)$, which in turn implies

$$\frac{f_{\mathrm{pu}}(2L)}{f_{\mathrm{pu}}(L)} = \frac{S_L}{S_{2L}}. \tag{21}$$

Following Refs. [6,12] the effective area of the modes of a planar dielectric cavity with length L, resonance wavelength λ and reflectivity R is given by $S_L = \pi L\lambda/1 - R$. Therefore,

$$\frac{f_{\mathrm{pu}}(2L)}{f_{\mathrm{pu}}(L)} = \frac{1}{2} \tag{22}$$

which agrees with our experimental observation in the long-time delay regime of the pump-probe response. Note that this result is quite unlike the usual pump-probe response of bare molecules. In electromagnetic environments where photon modes are unconfined, the above considerations would not apply and the effective mode areas corresponding to lengths L and 2L would be the same.

References:

1. Xiang, B. *et al.* Two-dimensional infrared spectroscopy of vibrational polaritons. *Proc. Natl. Acad. Sci.* **115,** 4845–4850 (2018).
2. Shim, S.-H. & Zanni, M. T. How to turn your pump-probe instrument into a multidimensional spectrometer: 2D IR and Vis spectroscopies via pulse shaping. *Phys. Chem. Chem. Phys.* **11,** 748–761 (2009).
3. Khitrova, G., Gibbs, H. M., Jahnke, F., Kira, M. & Koch, S. W. Nonlinear optics of normal-mode-coupling semiconductor microcavities. *Rev. Mod. Phys.* **71,** 1591–1639 (1999).
4. Long, J. P. & Simpkins, B. S. Coherent coupling between a molecular vibration and fabry-perot optical cavity to give hybridized states in the strong coupling limit. *ACS Photonics* **2,** 130–136 (2015).
5. Zhu, Y. *et al.* Vacuum Rabi splitting as a feature of linear-dispersion theory: Analysis and experimental observations. *Phys. Rev. Lett.* **64,** 2499–2502 (1990).
6. Ujihara, K. Spontaneous emission and the concept of effective area in a very short optical cavity with plane-parallel dielectric mirrors. *Jpn. J. Appl. Phys.* **30,** L 901-L 903 (1991).
7. Ribeiro, R. F. *et al.* Theory for Nonlinear Spectroscopy of Vibrational Polaritons. *J. Phys. Chem. Lett.* **9,** 3766–3771 (2018).
8. Kavokin, A., Baumberg, J. J., Malpuech, G. & Laussy, F. P. *Microcavities*. *Microcavities* (2008). doi:10.1093/acprof:oso/9780199228942.001.0001
9. Kakazu, K. & Kim, Y. S. Quantization of electromagnetic fields in cavities and spontaneous emission. *Phys. Rev. A* **50,** 1830–1839 (1994).
10. Ribeiro, R. F., Martínez-Martínez, L. A., Du, M., Campos-Gonzalez-Angulo, J. & Yuen-Zhou, J. Polariton chemistry: controlling molecular dynamics with optical cavities. *Chem. Sci.* (2018). doi:10.1039/c8sc01043a
11. Letokhov, V. S. *Principles of nonlinear optical spectroscopy*. *Physics-Uspekhi* **41,** (1998).
12. De Martini, F., M. Marrocco, and D. M. Transverse Quantum Correlations in the Active Microscopic Cavity. *Phys. Rev. Lett.* **65,** 1853 (1990).